



# Anatase TiO<sub>2</sub> nanocrystals anchored at inside of SBA-15 mesopores and their optical behavior



M.M. Araújo<sup>a,b</sup>, L.K.R. Silva<sup>a</sup>, J.C. Sczancoski<sup>c</sup>, M.O. Orlandi<sup>c</sup>, E. Longo<sup>c</sup>, A.G.D. Santos<sup>d</sup>, J.L.S. Sá<sup>a</sup>, R.S. Santos<sup>a</sup>, G.E. Luz Jr.<sup>a</sup>, L.S. Cavalcante<sup>a,\*</sup>

<sup>a</sup> PPGQ-GERATEC-CCN-DQ, Universidade Estadual do Piauí, João Cabral, N. 2231, P.O. Box 381, 64002-150 Teresina, PI, Brazil

<sup>b</sup> Departamento de Química (DQ), Universidade Federal do Piauí-UFPI, 64049-550 Teresina, PI, Brazil

<sup>c</sup> CDMF-Universidade Estadual Paulista, P.O. Box 355, 14801-907, Araraquara, SP, Brazil

<sup>d</sup> Departamento de Ciências Naturais, Universidade Estadual do Rio Grande do Norte, Mossoró, RN, Brazil

## ARTICLE INFO

### Article history:

Received 13 May 2016

Received in revised form 4 August 2016

Accepted 5 August 2016

Available online 8 August 2016

### Keywords:

SBA-15 mesopores

TiO<sub>2</sub> nanocrystals

Infrared

Growth mechanism

Optical band gap

## ABSTRACT

In this paper, a new synthesis method was proposed to obtain anatase titanium oxide (TiO<sub>2</sub>) nanocrystals anchored into SBA-15 molecular sieve, as a matrix assigned by the in-situ anchoring (ISA) method. Pure SBA-15 and modified with TiO<sub>2</sub> nanocrystals at different Si/Ti molar ratios ( $R = 75, 50, \text{ and } 25$ ) were structurally characterized by X-ray diffraction (XRD), Micro-Raman and Fourier Transform infrared (FTIR) spectroscopies. Specific surface area, pore volume and average pore diameter were estimated using both Brunauer-Emmett-Teller (BET) and Barrett-Joyner-Halenda (BJH) methods, respectively. Morphological aspects of these samples were observed by means of field emission scanning electron microscopy (FE-SEM) and transmission electron microscopy (TEM). Optical properties were investigated by ultraviolet-visible (UV-vis) diffuse reflectance spectroscopy. XRD patterns, Micro-Raman and FT-IR spectra indicate the TiO<sub>2</sub> nanocrystals crystallized in a tetragonal structure anchored into the SBA-15 mesopores. BET and BJH methods prove a large amount of TiO<sub>2</sub> nanocrystals were anchored inside of SBA-15 mesopores due to increase in surface area and average pore size of SBA-15 matrix. FE-SEM and TEM images showed the pure SBA-15 has an elongated hexagon-shaped microstructure, and an average size of 7.34 nm for 2D hexagonal mesopores. Moreover, ISA method was able to avoid blocking of mesopores, in addition promotes a significant increasing the impregnation rate of anatase TiO<sub>2</sub> nanocrystals in SBA-15 matrix. A growth mechanism was proposed in order to explain the stages involved in the formation of TiO<sub>2</sub>-SBA mesoporous. UV-vis spectra revealed a dependence of the optical band gap energy ( $E_{\text{gap}}$ ) with the decreasing of Si/Ti molar ratios.

© 2016 Elsevier B.V. All rights reserved.

## 1. Introduction

In 1990, Yanagisawa *et al.* [1] first investigated the single layered polysilicate kanemite and its conversion to microporous materials. This scientific study was of fundamental importance for the development of new synthetic routes focused in the preparation of mesoporous silica (SiO<sub>2</sub>) nanoparticles. Mesoporous SiO<sub>2</sub>, Mobil Crystalline Materials (MCM-41), and Santa Barbara Amorphous (SBA-15) are mesoporous materials well-known in the literature [2–4].

In the last years, researches have devoted their efforts in the study of SBA-15, which these molecular sieves because of their technological applications, such as drug delivery [5], biosensors

[6], thermal energy storage [7], luminescence [8,9], and biomedical imaging [10]. Particularly, especial attention has been devoted to SBA-15 because of its 2D hexagonal pore structure (average diameters between 2 and 10 nm), high surface area (typically >800 m<sup>2</sup>/g) [11,12], and high capacity for adsorption of toxic heavy metals {Cu(II), Zn(II), Cd(II), Ni(II), and Pb(II)} [13,14]. Moreover, as is an amorphous silica, pure SBA-15 does not exhibit an efficient catalytic activity due to absence of active sites in its structure.

In order to induce the formation of activity sites in pure SBA-15, especially catalytic sites, titanium oxide (TiO<sub>2</sub>) has been widely added in this mesoporous matrix for this purpose [14]. TiO<sub>2</sub> can be found naturally in three crystalline phases, as rutile, anatase, and brookite [15]. The rutile and anatase phases have tetragonal structure with space group ( $P4_2/mnm$ ) [16] and ( $I4_1/amd$ ), respectively [17]. The brookite phase crystallizes in an orthorhombic structure with space group TiO<sub>2</sub>/SBA-15 ( $Pcab$ ) [18]. Among these crystallographic phases, the anatase is the most investigated polymorphous

\* Corresponding author.

E-mail addresses: [laeciosc@gmail.com](mailto:laeciosc@gmail.com), [laeciosc@bol.com.br](mailto:laeciosc@bol.com.br) (L.S. Cavalcante).

in materials science because of its high catalytic and photocatalytic activities [19,20]. The anatase TiO<sub>2</sub> nanocrystals into the SBA-15 mesoporous has been employed for improving its electronic performance in humidity sensors [21], enhanced visible-light photoactivity [22,23], catalysts in cyclohexene epoxidation [24], fuel cell membrane [25], oxidation of carbon monoxide [26], as catalysts for direct propylene epoxidation with O<sub>2</sub> and H<sub>2</sub> mixtures [27], drug releaser [28].

In terms of preparation techniques, two methods are commonly employed for obtaining SBA-15 modified with TiO<sub>2</sub> nanocrystals: post-synthesis and one-pot methods. The first one is able to promote the formation of metal oxides in the channels or external surfaces of support, which could block the channels and not allows the easy access of reactant molecules to the reaction sites in the porous matrix [29–39]. In the second one, it occurs the simultaneous addition of the precursors of silica and titanium oxides in the synthesis gel. This method limits the amount of titanium oxide that can be incorporated, once the increase of the TiO<sub>2</sub> concentration promotes the distance of the SBA-15 characteristic because of the fast hydrolysis that occur in the titanium oxide precursors over the micelles of the template [40–42].

Therefore, the aim of this study was the preparation of SBA-15 matrices modified with anatase TiO<sub>2</sub> nanocrystals by the in-situ anchoring (ISA) method, in which was investigated the influence of different Si/Ti molar ratios ( $R=75, 50, \text{ and } 25$ ) on the structural behavior and optical properties.

## 2. Experimental procedure

### 2.1. Synthesis of pure SBA-15 matrix

The preparation conditions of mesoporous SBA-15 using direct synthesis method with pH adjustment have been reported in our previous papers [43,44]. A typical synthesis method of pure SBA-15 matrix is described as follows: 4 g of amphiphilic triblock copolymer, poly(ethylene glycol)-*block*-poly(propylene glycol)-*block*-poly(ethylene glycol), Pluronic P123 (average molecular weight 5800), 97% purity (Sigma-Aldrich), was dissolved in 148.3 mL of hydrochloric acid (HCl – Vetec) solution (pH < 0.1) under stirring for 2 h at 40 °C. In the sequence, 8.8 mL of tetraethyl orthosilicate (TEOS), 98% purity (Sigma-Aldrich), was added to initial mixture, which was maintained at 40 °C for 24 h under constant stirring. Thereafter, the formed gel was transferred to inside a Teflon cup (200 mL capacity), which was placed inside a stainless autoclave. This system was sealed and subjected to hydrothermal conditions performed at 100 °C for 48 h. The obtained samples were washed several times with ethanol, filtrated at vacuum, and heat treated at 500 °C for 5 h under air flow. This heat treatment was adopted to decompose the triblock copolymer and obtain the SBA-15.

### 2.2. Synthesis of anatase TiO<sub>2</sub> nanocrystals

Initially, 120 μL of nitric acid [HNO<sub>3</sub>] (65%, Vetec) was dissolved in 30 mL of deionized water (H<sub>2</sub>O) contained in a round-bottom flask, which was immersed in a thermostatic oil bath heated at 90 °C. Thereafter, 2.5 mL of titanium (IV) isopropoxide [Ti(OC<sub>3</sub>H<sub>7</sub>)<sub>4</sub>] (99%, Aldrich) was added in this solution. This system at 90 °C was maintained under reflux for 12 h up to obtain the anatase TiO<sub>2</sub> nanocrystals, as consequence of the total hydrolysis of Ti precursor. TiO<sub>2</sub> concentration was determined by means of gravimetric procedure.

### 2.3. Synthesis of anatase TiO<sub>2</sub> nanocrystals/SBA-15 powders

An adequate amount of anatase TiO<sub>2</sub> nanocrystals at colloidal state, necessary to reach a Si/Ti molar ratio of 75, was added into the Pluronic (P123) micelle dispersion, which was previously obtained by the Pluronic (P123) dispersion in HCl solution under stirring at 40 °C for 2 h, as was previously described in item 2.1. After the addition of TiO<sub>2</sub> nanocrystals, the mixture was maintained at 40 °C for more 2 h in order to anatase TiO<sub>2</sub> nanocrystals at colloidal state could be anchored and distributed on 2D-hexagonal shapes of lyotropic liquid-crystalline phase (P123 micelles). In the sequence, TEOS was added to this mixture and maintained at 40 °C for 24 h under stirring. This solution was subjected the hydrothermal treatment and washed in similar conditions to those described in item 2.1. The obtained sample was washed several times with ethanol, filtrated at vacuum, and heat treated at 500 °C for 5 h under air flow. Similar procedure was employed to obtain anatase TiO<sub>2</sub> nanocrystals/SBA-15 powders with Si/Ti molar ratio ( $R$ ) = 50 and 25.

### 2.4. Characterization

Pure SBA-15 matrix, anatase TiO<sub>2</sub> nanocrystals and TiO<sub>2</sub>/SBA-15 were structurally characterized by means of XRD using a LabX XRD-6000 diffractometer (Shimadzu, Japan) with Cu K $\alpha$  radiation ( $\lambda = 0.15406 \text{ nm}$ ) in the  $2\theta$  range at low angle from 0.5° to 4.0° and at wide angle from 10° to 80°, both with a scanning velocity of 2°/min. Micro-Raman spectra were recorded using a SENTERRA spectrometer (Bruker, Germany) equipped with He-Ne laser ( $\lambda = 532 \text{ nm}$ ) and CCD operating from 85 cm<sup>-1</sup> to 800 cm<sup>-1</sup> with spectral resolution of 4 cm<sup>-1</sup>. The incident laser beam power on the sample was maintained at 20 mW. A 50 μm lens was used to prevent overheating the samples. The specific surface area analyses with nitrogen adsorption and desorption were recorded in an ASAP-2420 equipment (Micromeritics, USA). For each analysis were used approximately 30 mg of each calcined sample, which were previously degassed at 300 °C for 3 h. The isotherms were obtained in a range of relative pressure ( $P/P_0$ ) from 0.01 to 0.99 at temperature of the liquid nitrogen (77 K). The surface areas were estimated by the Brunauer, Emmett and Teller (BET) method [45], while the pore volumes and average pore diameters were estimated by the Barrett, Joyner and Halenda (BJH) method [46]. The composition was obtained with an Epsilon 1 HP-EDXRF spectrometer (PANalytical, Netherlands) equipped with a Rh anode X-ray tube (600 W), using a voltage of 50 kV and a current of 30 mA. Morphological aspects were observed with a Quanta 250 field-emission scanning electron microscopy (FE-SEM) (FEI Company, Netherlands) operated at 10 kV and, using a transmission electron microscopy (TEM) model CM200 (Philips, Netherlands) operated at 200 kV. The samples for the TEM were prepared by the immersion of copper grids in dilute solutions of obtained powders in ethanol. UV–vis diffuse reflectance spectra were taken using an UV-2600 spectrophotometer (Shimadzu, Japan). The optical band gap energy ( $E_{gap}$ ) was calculated using the method proposed by Kubelka and Munk for indirect electronic transitions [46,47].

## 3. Results and discussion

### 3.1. X-ray diffraction patterns analyses

Fig. 1(a) and (b) illustrate the XRD patterns at low and wide angles of pure SBA-15 matrix and modified with TiO<sub>2</sub> nanocrystals at different Si/Ti molar ratios ( $R=75, 50, \text{ and } 25$ ), respectively.

In Fig. 1(a), all XRD patterns performed at low angle showed three diffraction peaks ( $2\theta \cong 0.80^\circ, 1.44^\circ, \text{ and } 1.67^\circ$ ) related to

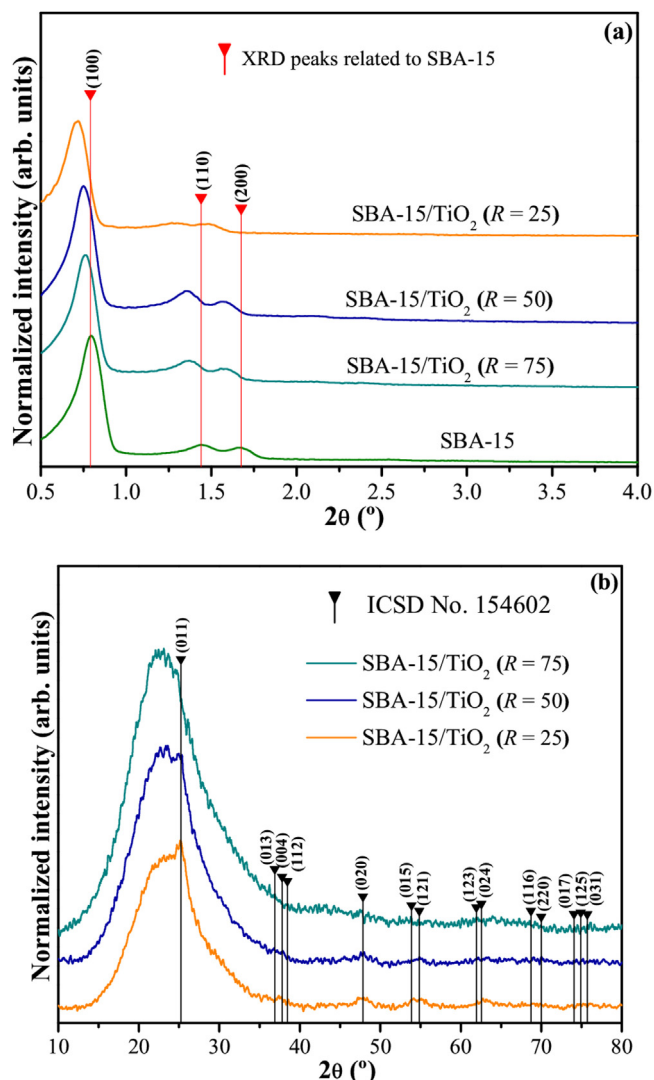


**Fig. 1.** XRD patterns at (a) low angle ( $0.5^{\circ}$ – $4^{\circ}$ ) and (b) wide angle ( $10^{\circ}$ – $80^{\circ}$ ) of pure SBA-15 and  $\text{TiO}_2/\text{SBA-15}$  at different Si/Ti molar ratios ( $R = 75, 50, 25$ ). The vertical lines indicate the positions and intensities of diffraction peaks of SBA-15 and ICSD card No. 154602 for the anatase  $\text{TiO}_2$  phase, respectively.

(100), (210) and (200) crystallographic planes, respectively. These peaks can be assigned to ordered 2D hexagonal mesostructure with space group ( $P6mm$ ) and point group symmetry ( $C_{6v}$ ) [48], in good agreement with the data reported in International Tables for Crystallography (ITC) n° 183 [49,50]. This pattern is characteristic of SBA-15 structure [40,41], which indicates that the in-situ anchoring (ISA) preparation method, employed in this study, did not destroy the structural mesoporous of SBA-15. In addition, it is important to highlight that these three diffraction peaks are shifted to lower  $2\theta$  values for  $\text{TiO}_2/\text{SBA-15}$  samples in relation to pure SBA-15 matrix, indicating there is an increase in the unit-cell parameters [51], which may be related the incorporation of  $\text{TiO}_2$  nanocrystals into the SBA-15 mesoporous walls.

For XRD patterns obtained at wide angle, some low intensity diffraction peaks were identified, which are ascribed to anatase  $\text{TiO}_2$  phase with tetragonal structure, space group ( $I4_1/amd$ ), lattice parameters ( $a = 3.824(3)\text{Å}$  and  $c = 9.581(4)\text{Å}$ ) and four molecular formula per unit cell ( $Z = 4$ ) [52,53]. The intense and broad XRD peak located at around  $23.5^{\circ}$  is characteristic of amorphous silica ( $\text{SiO}_2$ ) [54].

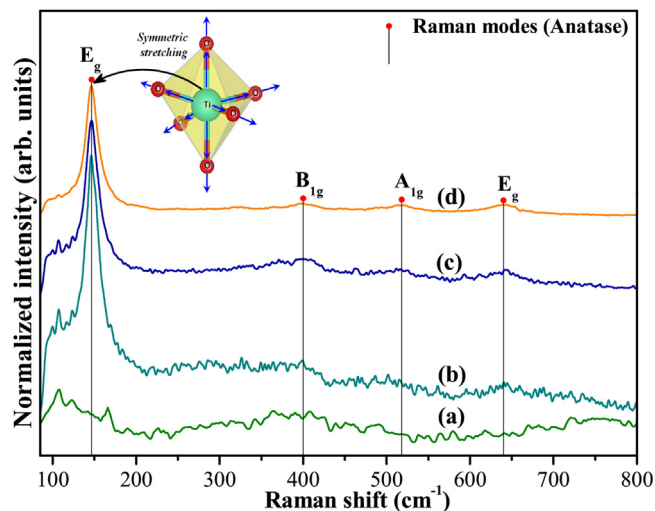


**Fig. 2.** Micro-Raman spectra of (a) pure SBA-15 matrix, (b)  $\text{TiO}_2/\text{SBA-15}$  ( $R = 75$ ), (c)  $\text{TiO}_2/\text{SBA-15}$  ( $R = 50$ ) and (d)  $\text{TiO}_2/\text{SBA-15}$  ( $R = 25$ ). The vertical lines indicate the relative positions of Raman-active modes for the anatase  $\text{TiO}_2$  phase and inset shows the symmetric stretching of ( $\leftarrow\text{O}\leftarrow\text{Ti}\rightarrow\text{O}\rightarrow$ ) bonds.

### 3.2. Micro-Raman spectroscopy analyses

Fig. 2(a–d) illustrates the micro-Raman spectra of pure SBA-15 matrix and modified with  $\text{TiO}_2$  nanocrystals at different Si/Ti molar ratios ( $R = 75, 50$ , and  $25$ ), respectively.

Raman spectra of pure SBA-15 matrix are similar to those previously published in other papers [55–57]. Raman-active bands have lower intensities, which are assigned to O–Si–O symmetric vibrational modes, arising from isolated four-membered rings of tetrahedral [ $\text{SiO}_4$ ] clusters, and breathing vibrations of three-membered rings of tetrahedral [ $\text{SiO}_4$ ] clusters [57]. However, as can be noted in Fig. 2(b–d), the increase in the amount of  $\text{TiO}_2$  nanocrystals into the SBA-15 matrix promoted the slight appearance of Raman modes at  $147\text{ cm}^{-1}$ ,  $400\text{ cm}^{-1}$ ,  $518\text{ cm}^{-1}$ , and  $640\text{ cm}^{-1}$ , which are related to  $\text{TiO}_2$  anatase phase.

Particularly, the Raman spectrum of  $\text{TiO}_2/\text{SBA-15}$  ( $R = 25$ ) revealed the presence of four active bands ( $2E_g$ ,  $1B_{1g}$ , and  $1A_{1g}$ ) associated to anatase  $\text{TiO}_2$  nanocrystals (Fig. 4(d)). The  $E_g$  mode at  $147\text{ cm}^{-1}$  is ascribed to symmetric stretching vibration ( $\leftarrow\text{O}\leftarrow\text{Ti}\rightarrow\text{O}\rightarrow$ ) in octahedral [ $\text{TiO}_6$ ] clusters, while the  $B_{1g}$  mode at  $400\text{ cm}^{-1}$  is related to symmetric bending vibration ( $\sphericalangle\text{O}\sphericalangle\text{Ti}\sphericalangle\text{O}\sphericalangle$ ) in these same kinds of clusters. The  $A_{1g}$  mode at  $518\text{ cm}^{-1}$  is assigned to anti-symmetric bending vibration ( $\sphericalangle\text{O}\sphericalangle\text{Ti}\sphericalangle\text{O}\sphericalangle$ ). Finally,  $E_g$  mode at  $640\text{ cm}^{-1}$  is attributed to displacement of symmetric oxygen atoms in Ti–O bonds in the  $x,y$ -plane ( $\leftarrow\text{O}\leftarrow\text{Ti}\rightarrow\text{O}\rightarrow$ ), which is in good agreement with the studies reported by Yan et al. [58], and Exarhos et al. [59]. Moreover, the other two Raman-active vibration modes ( $1B_{1g}$  and  $1E_g$ ) were not detectable because of their lower intensities [60,61].

### 3.3. Fourier transform-infrared spectroscopy analyses

Fig. 3 (a–d) illustrates the FT-IR spectra of pure SBA-15 matrix and modified with  $\text{TiO}_2$  nanocrystals at different Si/Ti molar ratios ( $R = 75, 50$ , and  $25$ ), respectively.

FT-IR spectroscopy was employed to monitor the incorporation of  $\text{TiO}_2$  nanocrystals into the SBA-15 matrix [62]. In the region from  $400\text{ cm}^{-1}$  to  $2000\text{ cm}^{-1}$ , these spectra revealed six IR-active vibration modes due to Si–O bonds or Si–OH groups. The spectra in Fig. 3(b–d) showed some significant changes in relation to IR spectrum of pure SBA-15 matrix (Fig. 3(a)), in which the bands are typical of O–Ti–O–Si–O bonds. The first IR-active mode at around

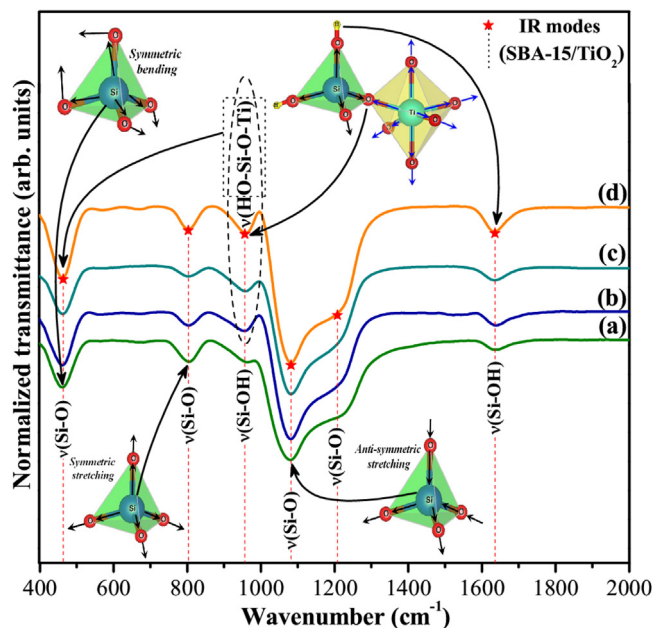


**Fig. 3.** FT-IR spectra of (a) pure SBA-15 matrix, (b)  $\text{TiO}_2/\text{SBA-15}$  ( $R=75$ ), (c)  $\text{TiO}_2/\text{SBA-15}$  ( $R=50$ ) and (d)  $\text{TiO}_2/\text{SBA-15}$  ( $R=25$ ). The vertical lines indicate the relative positions of IR-active modes for the anatase  $\text{TiO}_2$  phase and insets show the symmetric stretching of ( $\leftarrow\text{O}\leftarrow\text{Si}\rightarrow\text{O}\rightarrow$ ) bonds; symmetric bending of ( $\swarrow\text{O}\swarrow\text{Si}\searrow\text{O}\searrow$ ) bonds; anti-symmetric stretching ( $\swarrow\text{O}\swarrow\text{Si}\searrow\text{O}\searrow$ ) bonds and possible symmetric stretching of ( $\leftarrow\text{O}\leftarrow\text{Si}\rightarrow\text{O}\leftarrow\text{TiO}\rightarrow$ ) bonds.

$460\text{ cm}^{-1}$  is related to symmetric bending vibrations of  $\nu(\text{Si}-\text{O})$  bonds because of twisting motion in tetrahedral  $[\text{SiO}_4]$  clusters (Inset in Fig. 3(a)) [63]. The second IR-active mode at  $804\text{ cm}^{-1}$  is ascribed to symmetric stretching vibrations of  $\nu(\text{Si}-\text{O})$  bonds in tetrahedral  $[\text{SiO}_4]$  clusters [64]. The third IR-active mode

at  $960\text{ cm}^{-1}$  is caused by the symmetric stretching vibrations of  $\nu(\text{Si}-\text{OH})$  bonds in silanol groups [65]. Moreover, it was noted an increase in the intensity of this respective band with the addition of Ti atoms into the SBA-15 matrix. This behavior is possibly due to strong chemical bonds ( $\text{HO}-\text{Si}-\text{O}-\text{Ti}-\text{O}$ ) involving both octahedral  $[\text{TiO}_6]$  clusters (from  $\text{TiO}_2$  nanocrystals) and tetrahedral  $[\text{SiO}_4]$  clusters (from SBA-15) [66]. The fourth IR-active mode at  $1082\text{ cm}^{-1}$  is arising from anti-symmetric stretching vibrations of  $\nu(\text{Si}-\text{O})$  bonds in  $[\text{SiO}_4]$  clusters [67]. According to de Sousa et al. [68], the fifth IR-active mode (shoulder at  $1208\text{ cm}^{-1}$ ) is corresponding to anti-symmetric stretching vibrations of  $\nu(\text{Si}-\text{O})$  bonds. Finally, IR-active mode at  $1636\text{ cm}^{-1}$  is associated to bending vibrations of  $\nu(\text{Si}-\text{OH})$  bonds, which is arising from the adsorbed water on the SBA-15 surface [69].

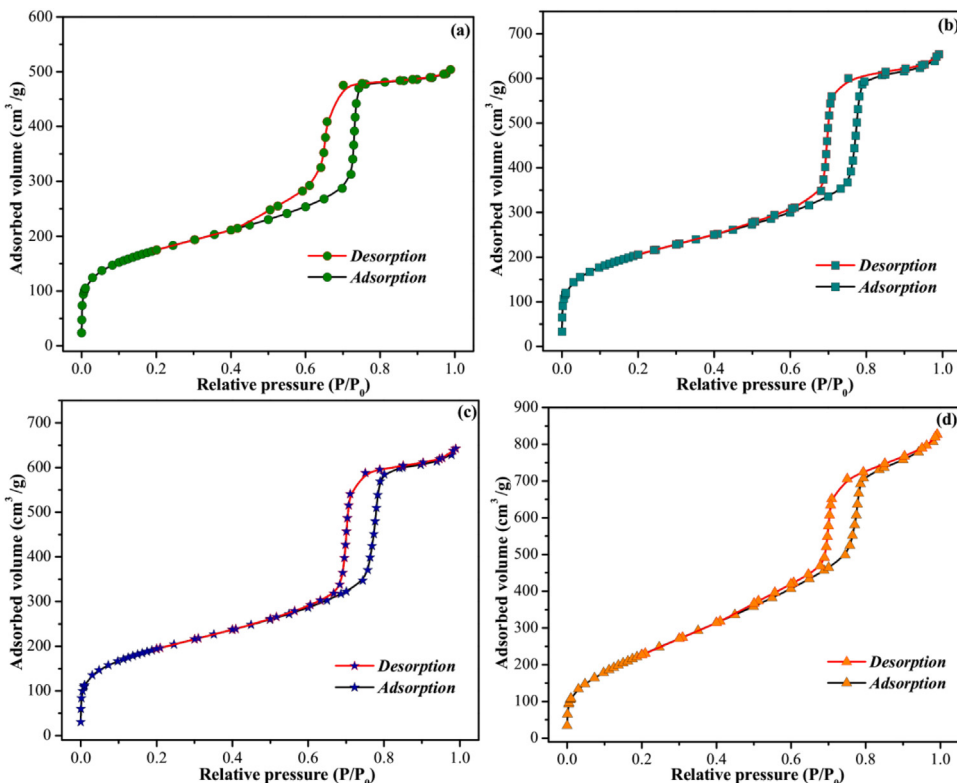
#### 3.4. $\text{N}_2$ adsorption/desorption analyses

Fig. 4(a–d) illustrate the  $\text{N}_2$  adsorption/desorption isotherms of pure SBA-15 matrix and modified with  $\text{TiO}_2$  nanocrystals at different Si/Ti molar ratios ( $R=75$ , 50, and 25), respectively.

All samples exhibited a typical irreversible type-IV adsorption/desorption isotherm with a H1 hysteresis loop, as defined by the International Union of Pure and Applied Chemistry (IUPAC) [70]. These isotherm profiles are typical features of mesoporous materials with cylindrical pores, like the SBA-15 [43,44], and are in agreement with XRD results. Furthermore, indicate that  $\text{TiO}_2$  nanocrystals employing by in-situ anchoring (ISA) method did not block the mesoporous of SBA-15 matrix.

Fig. 5(a–d) shows the structure of the pore size distribution for pure SBA matrix and SBA-15 matrix modified with  $\text{TiO}_2$  nanocrystals.

As it can be noted in Fig. 5(a), the pure SBA-15 matrix exhibits a very narrow pore size distribution with an average diameter of 6.5 nm. However, the anchoring of some  $\text{TiO}_2$  nanocrystals in



**Fig. 4.**  $\text{N}_2$  adsorption-desorption isotherms of (a) pure SBA-15 matrix, (b)  $\text{TiO}_2/\text{SBA-15}$  ( $R=75$ ), (c)  $\text{TiO}_2/\text{SBA-15}$  ( $R=50$ ) and (d)  $\text{TiO}_2/\text{SBA-15}$  ( $R=25$ ).

**Table 1**

Specific surface area and pore size distribution parameters and textural properties of pure SBA matrix and SBA-15 matrix modified with TiO<sub>2</sub> nanocrystals at different Si/Ti molar ratios, in short as: TiO<sub>2</sub>/SBA-15 (*R* = 75, 50, 25), respectively.

Samples	$S_{\text{BET}}$ (m <sup>2</sup> g <sup>-1</sup> )	$S_{\text{micro}}$ (m <sup>2</sup> g <sup>-1</sup> )	$V_{\text{poro}}$ (cm <sup>3</sup> g <sup>-1</sup> )	$V_{\text{micro}}$ (cm <sup>3</sup> g <sup>-1</sup> )	<sup>a</sup> Dp (nm)	$a_0$ (nm)	<sup>b</sup> w (nm)
SBA-15	624.1	126.8	0.78	0.05	6.39	12.91	6.52
TiO <sub>2</sub> /SBA-15( <i>R</i> = 75)	738.8	126.9	1.01	0.05	7.22	14.17	6.95
TiO <sub>2</sub> /SBA-15( <i>R</i> = 50)	697.6	115.8	0.99	0.05	7.36	13.6	6.24
TiO <sub>2</sub> /SBA-15( <i>R</i> = 25)	858.1	0	1.28	0	5.90	13.42	7.52

<sup>a</sup> BJH pore diameter calculated from the adsorption branch.

<sup>b</sup>  $w = a_0 - D_p$ .

mesoporous SBA-15 promoted a broadening in pore size distribution, and an increasing in average diameter to 7.2 nm (Fig. 5(b, c)). The increase in the addition of TiO<sub>2</sub> nanocrystals in SBA-15 matrix resulted in a reduction in average pore size to 5.9 nm (Fig. 5(d)). Furthermore, it can be checked one shoulder on the bimodal pore distribution, which can be attributed to the presence of internal aggregates of TiO<sub>2</sub> nanocrystals inside the mesopores formed by the calcination process [71]. In Table 1 are listed the specific surface area and porosity calculated by the BET and BJH methods, respectively.

In this table, TiO<sub>2</sub>/SBA-15 (*R* = 25) sample has a high value for both specific surface area and pore volume in relation to pure SBA-15 matrix and other synthesized samples. This behavior can be designed to formation of homogeneous distribution of TiO<sub>2</sub> nanocrystals into the mesoporous SBA-15 matrix by the proposed ISA method. These results indicate that the decrease of Si/Ti molar ratios (*R* = 75 → 25) is ideal to promote an increase in the wall thickness.

The textural properties obtained from isotherms and XRD patterns are shown in Table 1. Analyzing these results, it is possible to note TiO<sub>2</sub>/SBA-15 has larger average pore size than the pure SBA-15, except the TiO<sub>2</sub>/SBA-15 (*R* = 25), as beforehand observed in Fig. 5. This fact can be related to the existence of TiO<sub>2</sub> nanocrystals into the SBA-15 mesopores walls [72], intercalated with SiO<sub>2</sub> groups. In fact, this behavior also can be because the Ti–O bonds are longer than the Si–O bonds (c.a. 0.21 Å). Moreover, both wall thickness and micropores area of these samples [TiO<sub>2</sub>/SBA-15 (*R* = 75, 50)] did not changed when compared to pure SBA-15.

TiO<sub>2</sub>/SBA-15 (*R* = 25) sample has larger wall thickness, and lower average pore size in relation to SBA-15, which can be attributed to agglomeration of TiO<sub>2</sub> nanocrystals. Consequently, this phenomenon is able to promote the formation of a thin layer, blocking the micropores entrance of this sample, as indicated in Table 1.

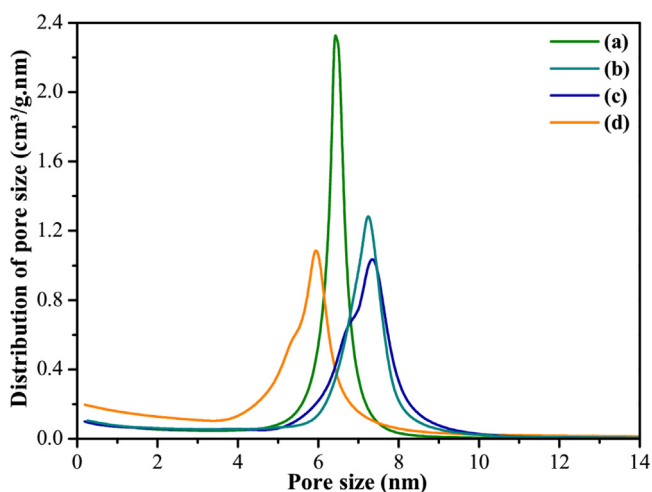


**Fig. 5.** Pore size distribution curves for: (a) pure SBA-15 matrix, (b) TiO<sub>2</sub>/SBA-15 (*R* = 75), (c) TiO<sub>2</sub>/SBA-15 (*R* = 50) and (d) TiO<sub>2</sub>/SBA-15 (*R* = 25).

**Table 2**

XRF data obtained for pure SBA matrix and SBA-15 matrix modified with TiO<sub>2</sub> nanocrystals at different Si/Ti molar ratios, in short as: TiO<sub>2</sub>/SBA-15 (*R* = 75, 50, 25), respectively.

Samples	Si/Ti molar ratio in synthesis	Si/Ti molar ratio by XRF
TiO <sub>2</sub> /SBA-15 SBA-15/TiO <sub>2</sub> ( <i>R</i> = 75)	75	36.9
TiO <sub>2</sub> /SBA-15 SBA-15/TiO <sub>2</sub> ( <i>R</i> = 50)	50	23.4
TiO <sub>2</sub> /SBA-15 SBA-15/TiO <sub>2</sub> ( <i>R</i> = 25)	25	10.9

These behaviors can indicate that the increase of the amount of TiO<sub>2</sub> nanocrystals (decrease of Si/Ti molar ratio) promotes the saturation of surface micelles of the Pluronic P123 template during the synthesis. Therefore, in TiO<sub>2</sub>/SBA-15 (*R* = 25), silanol groups condense on the thin layer of TiO<sub>2</sub> nanocrystals and not only on the micelles, resulting in an increase in wall thickness and micropores entrance blocking.

The fluorescence data, presented in Table 2, revealed that the TiO<sub>2</sub>/SBA-15 (*R*) samples have a Si/Ti molar ratio approximately two times lower than the theoretical value. This fact reinforces the idea that TiO<sub>2</sub> nanocrystals deposited on micelles may take a place of silanol groups during the synthesis. In addition, this result shows that the proposed ISA method may solve the problem of limitation of amount of active phase, especially metal oxide that can be incorporated in the SBA-15 molecular sieve [40–42].

### 3.5. Field-emission scanning electron microscopy images analyses

FEG-SEM images were of fundamental importance to understand the morphological evolution of SBA-15 with the increase of the amount of TiO<sub>2</sub> nanocrystals (*R* = 75 → 25) into the mesoporous by the proposed synthesis method in our study. Fig. 6(a–d) show the FE-SEM images of pure SBA-15 and SBA-15 samples modified with TiO<sub>2</sub> nanocrystals in different molar ratios, respectively.

In Fig. 6(a), the pure SBA-15 matrix has similar shape to irregular elongated tubes with different diameters and lengths. In addition, there are some interconnections between these tubes, which can be related to growth mechanism by means of self-assembly [73]. In Fig. 6(b), it is possible to confirm the shape of pure SBA-15 after incorporation the anatase TiO<sub>2</sub> nanocrystals in the pre-synthesis. Therefore, elongated hexagon can be observed in this FE-SEM image, confirming to the existence of highly ordered 2D hexagonal mesostructure with several mesopores. The presence of curves can be verified in these hexagons (Fig. 6(c)). Moreover, due to the new synthesis method proposed in this work, it is not possible to observe the presence of anatase TiO<sub>2</sub> nanocrystals on the surface of pure SBA-15 matrix (Fig. 6(c–d)). According to the literature [74], the curved shape of pure SBA-15 matrix is ascribed to the vortex effect and shearing force during the stirring process. When Si/Ti molar ratio was decreased, changes in the growth direction and shape of elongated hexagons were observed. In this case, it was noted the appearing of several twist in hexagon-like SBA-15 (Fig. 6(d)).

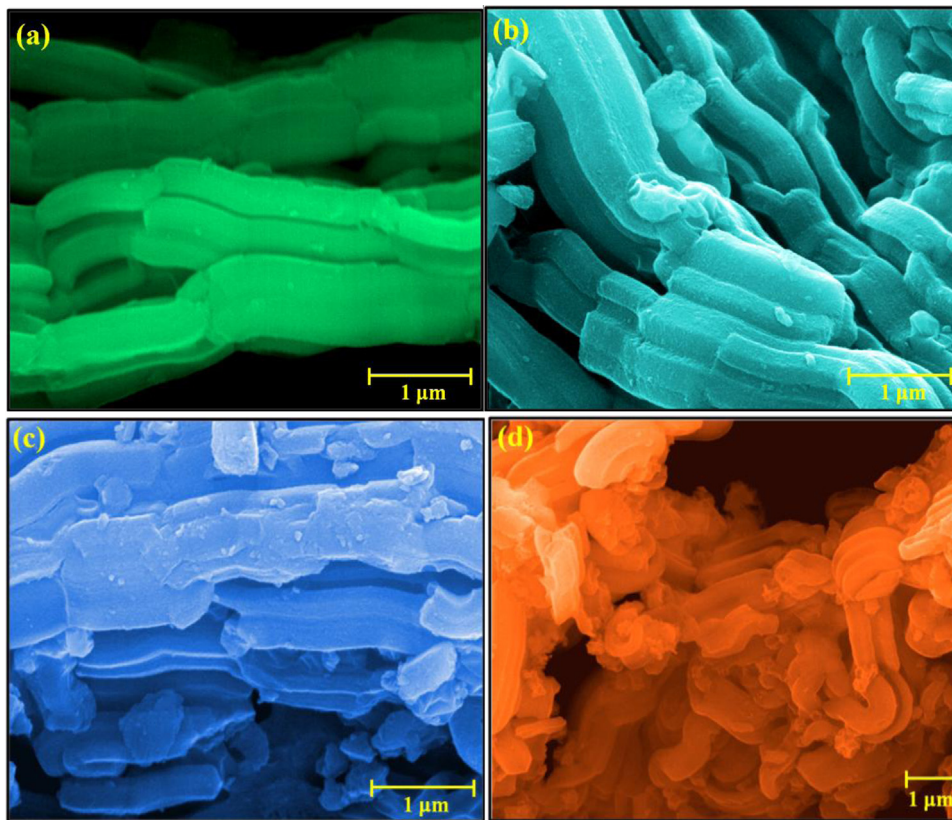


**Fig. 6.** FE-SEM images of (a) pure SBA-15 matrix, (b)  $\text{TiO}_2/\text{SBA-15}$  ( $R=75$ ), (c)  $\text{TiO}_2/\text{SBA-15}$  ( $R=50$ ) and (d)  $\text{TiO}_2/\text{SBA-15}$  ( $R=25$ ).

### 3.6. Transmission electron microscopy images analyses

TEM images were employed to monitor the anchoring of  $\text{TiO}_2$  nanocrystals into the SBA-15 matrix. Fig. 7(a–d) illustrate TEM

images of pure SBA-15 and SBA-15 samples modified with  $\text{TiO}_2$  nanocrystals, respectively.

Fig. 7(a) shows a high magnification TEM images performed on the edge of an elongated tube. SAED confirmed the SBA-15 matrix is composed of several mesopores (red circle in Fig. 7(a)), which

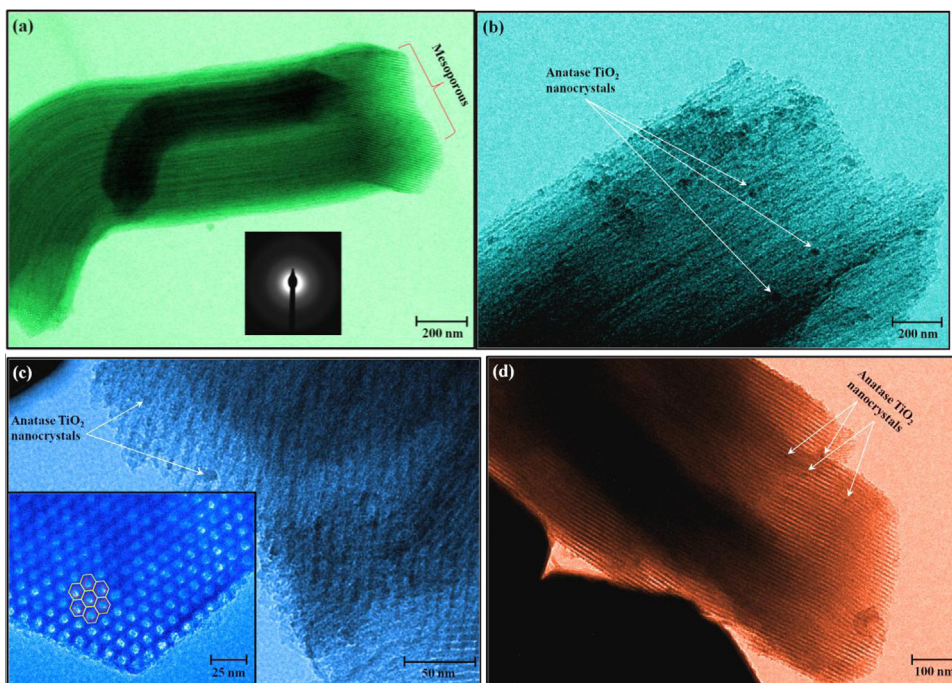


**Fig. 7.** TEM images of (a) pure SBA-15 matrix (Inset shows the selected area electron diffraction (SAED) of SBA-15), (b)  $\text{TiO}_2/\text{SBA-15}$  ( $R=75$ ), (c)  $\text{TiO}_2/\text{SBA-15}$  ( $R=50$ ) (Inset shows the HR-TEM for 2D hexagonal mesopores) and (d)  $\text{TiO}_2/\text{SBA-15}$  ( $R=25$ ).

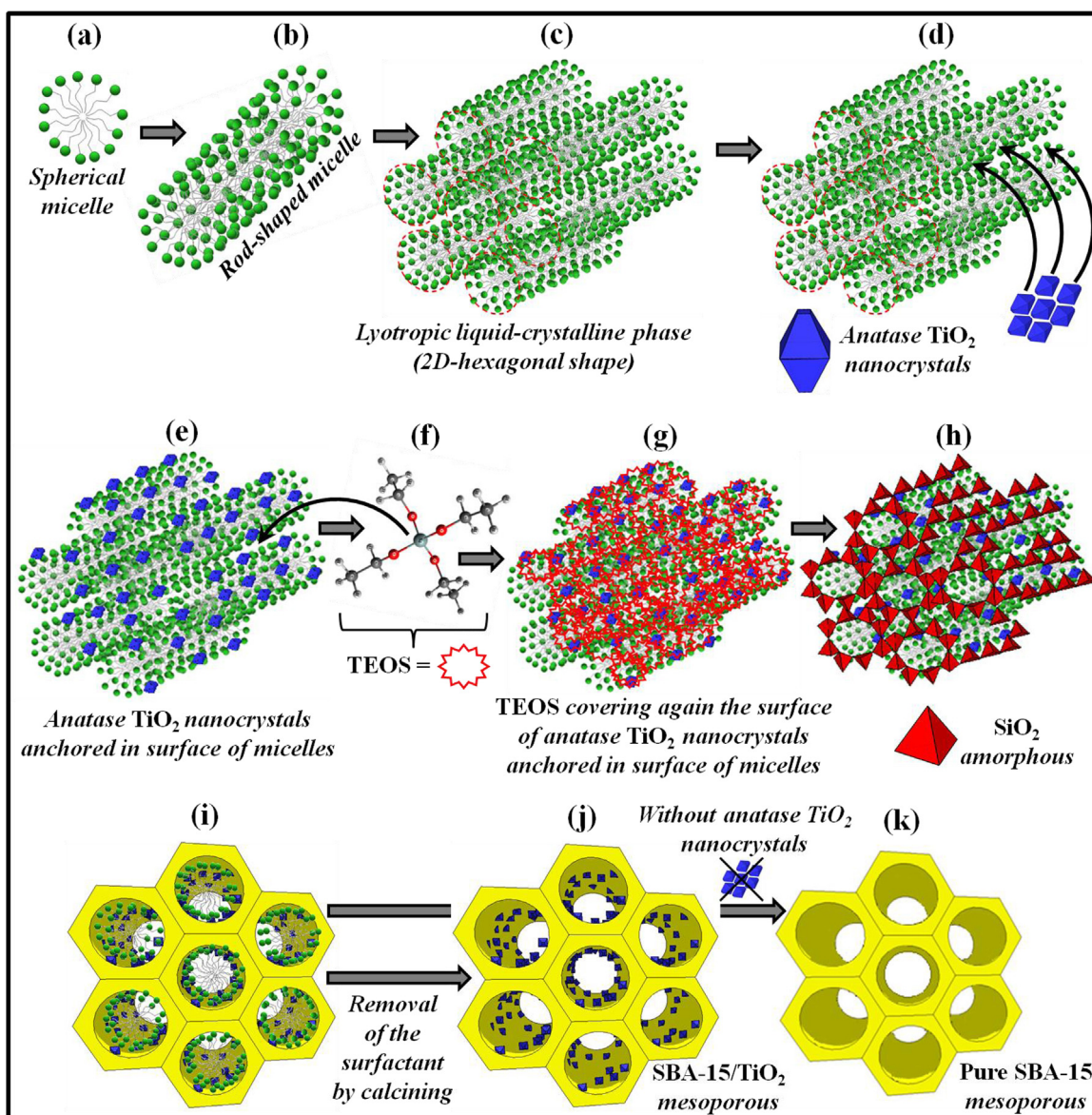


**Fig. 8.** A proposed growth mechanism of  $\text{TiO}_2/\text{SBA-15}$  and pure SBA-15 matrix: (a) Formation of sphere-like micelles; (b) Self-assembly of sphere-like micelles; (c) self-assembly cooperative of rod-shaped micelle, forming lyotropic liquid-crystalline phase; (d) anatase  $\text{TiO}_2$  nanocrystals added in lyotropic liquid-crystalline phase; (e) anatase  $\text{TiO}_2$  nanocrystals anchored on the surface of the micelles in the lyotropic liquid-crystalline state; (f) addition of TEOS in this system, (g) Surface coating of system already anchored with anatase  $\text{TiO}_2$  nanocrystals by the TEOS; (h) The hydrothermal process resulted in the formation of a precursor inorganic mesostructured solid-surfactant; (i) Composite inorganic mesostructured  $\text{TiO}_2/\text{SBA-15}/\text{surfactant}$  and, after the heat treatment, occurs the formation of (j) SBA-15 mesoporous silica/ $\text{TiO}_2$  nanocrystals and (k) pure SBA-15 mesoporous silica.

is commonly found in amorphous materials [73]. The presence of several small dark points (indicated by white arrows) inside the pores of SBA-15 matrix in Fig. 7(b), which are due to anatase  $\text{TiO}_2$  nanocrystals have average crystal size at about 7.2 nm anchored inside the mesoporous (see Support Information Fig. S1(a,b) and Fig. S2(a,b)). Moreover, TEM images revealed the presence of some anatase  $\text{TiO}_2$  nanocrystals inside the SBA-15 pore walls (white arrows in Fig. 7(c)), which is in good agreement with the discussion on textural properties shown in Table 1. High-resolution (HR)-TEM images is displayed in inset in Fig. 7(c) shows the well-ordered 2D hexagonal arrangement of SBA-15 mesopores. The uniform nanopores have a narrow pore size distribution with average size at 7.5 nm. Finally, as can be observed in Fig. 7(d), there is a large amount of small dark points inside the SBA-15 framework due to

anatase  $\text{TiO}_2$  nanocrystals. These results are in good agreement with the results reported by Chang *et al.* [75].

### 3.7. Growth mechanism of anatase $\text{TiO}_2$ nanocrystals/SBA-15 and pure SBA-15 matrix

Fig. 8(a–k) illustrate a schematic representation of all stages involved during the synthesis and growth of SBA-15 mesoporous silica/anatase  $\text{TiO}_2$  nanocrystals and SBA-15 mesoporous silica.

Initially, Fig. 8(a) shows the formation of typical sphere-like micelles in aqueous dispersion, when Pluronic P-123 surfactant was dispersed in water. In this stage, we have self-organization of several micelles with the hydrophilic “head” in contact with surrounding solvent ( $\text{H}_2\text{O}$ ), sequestering the hydrophobic single “tail” in the micelle center [76]. In Fig. 8(b) is illustrated the self-assembly

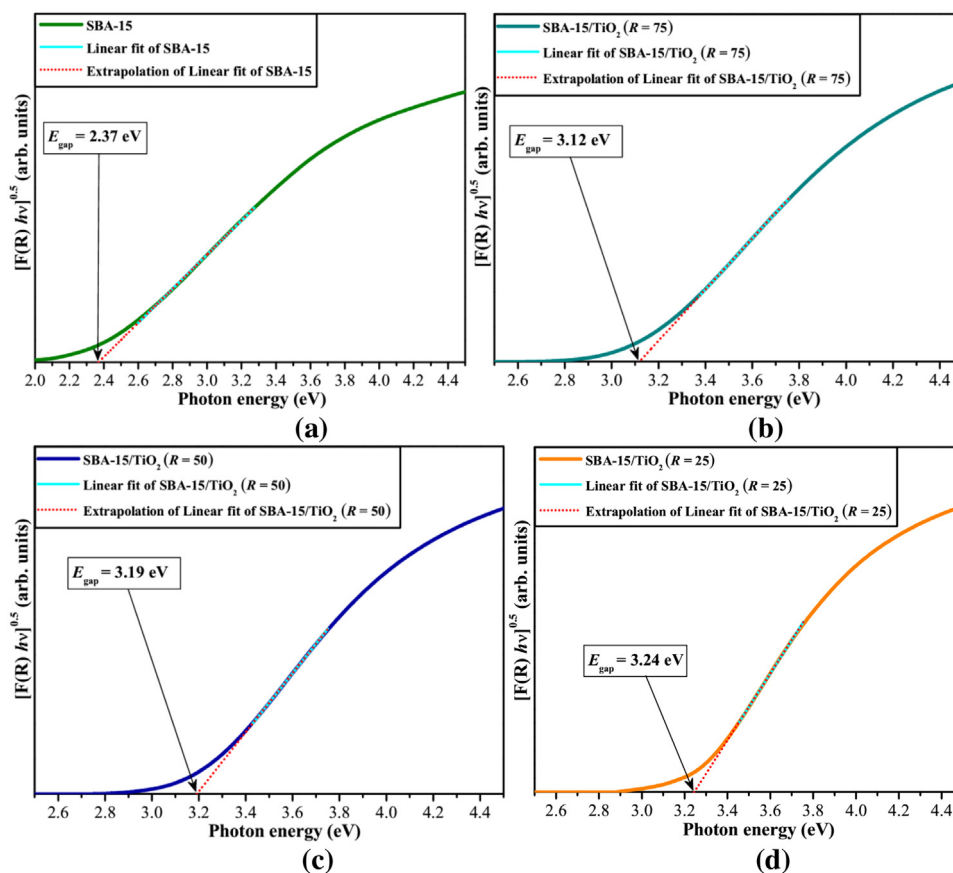


Fig. 9. UV-vis diffuse reflectance spectra of (a) pure SBA-15 matrix, (b)  $\text{TiO}_2/\text{SBA-15}$  ( $R = 75$ ), (c)  $\text{TiO}_2/\text{SBA-15}$  ( $R = 50$ ) and (d)  $\text{TiO}_2/\text{SBA-15}$  ( $R = 25$ ).

process of several sphere-like micelles with the formation of rod-like micelles. This effect is a typical feature of tri-block copolymer micelles (Pluronic P-123) [77], which display a similar behavior of surfactant micelles, acting as dynamic micelles and presenting a slow controlled diffusion process [78,79]. The high concentrations of Pluronic P-123 employed in this synthesis method promoted the fusion of rod-like micelles, forming cylindrical aggregates with different lengths (Fig. 8(c)), which are known as lyotropic liquid-crystalline phase (2D-hexagonal shape) [80,81]. In the sequence,  $\text{TiO}_2$  nanocrystals at colloidal state prepared by the reflux method at  $90^\circ\text{C}$  for 12 h were added at different molar ratios in this lyotropic liquid-crystalline phase (LL-CP) (Fig. 8(d)). Ideally, this procedure enables a homogeneous distribution of  $\text{TiO}_2$  nanocrystals on the LL-CP surface, as shown in Fig. 8(e). In a next stage, TEOS was added as an amorphous silica ( $\text{SiO}_2$ ) precursor (Fig. 8(f)). After several hours of chemical reaction performed at  $100^\circ\text{C}$ , TEOS covered completely the surface of  $\text{TiO}_2$  nanocrystals anchored on the LL-CP (Fig. 8(g)). Finalized the hydrothermal treatment, the composite inorganic mesostructured  $\text{TiO}_2/\text{SBA-15}/\text{surfactants}$  at different molar ratios ( $R = 75, 50$  and  $25$ ) were formed. This precursor is composed of LL-CP with some octahedron-like  $\text{TiO}_2$  nanocrystals, and several tetrahedral  $[\text{SiO}_4]$  clusters due to  $\text{SiO}_2$  amorphous (Fig. 8(h)). A composite inorganic mesostructured  $\text{TiO}_2/\text{SBA-15}/\text{organic surfactant}$  was formed after several washing and filtration processes (Fig. 8(i)). The heat treatment performed at  $550^\circ\text{C}$  promoted the complete removal of organic surfactants as well as the growth by self-assemble of several hexagonal mesoporous along the  $c$ -axis [82]. This procedure resulted in the formation of SBA-15 mesoporous silica/ $\text{TiO}_2$  nanocrystals (Fig. 8(j)) and pure SBA-15 mesoporous silica (Fig. 8(k)).

### 3.8. UV-vis diffuse reflectance spectroscopy analyses

Fig. 9(a–d) show the UV-vis diffuse reflectance spectra of all samples described in the present study.

As observed in Fig. 9(a–d),  $E_{\text{gap}}$  values increased when the Si/Ti molar ratio was decreased in  $\text{TiO}_2/\text{SBA-15}$ . In principle, this behavior is related to decrease of intermediary energy levels between the VB and CB. Particularly, the exponential optical absorption edge and the optical band gap energy are controlled by the degree of structural order–disorder in the lattice. The results showed the Ti as doping element increased the reflectance of visible light and extend the absorption edge to shorter wavelengths [83,84]. In addition,  $\text{SiO}_2$  amorphous exhibits only some electronic Si ( $3p$ ) and O ( $2p$ ) states, while the  $\text{TiO}_2/\text{SBA-15}$  samples have new electronic Ti ( $3d$ ) states, increasing the optical band gap.

### 3.9. Optical band gap model analyses

Fig. 10(a, b) shows the optical band gap model for pure SBA-15 related to  $\text{SiO}_2$  and anatase  $\text{TiO}_2$  nanocrystals/SBA-15 mesoporous, respectively.

As previously described in the text, the pure SBA-15 matrix is an amorphous silica; therefore, despite of its low degree of crystallinity at long-range (Fig. 1), there is a local-order (Fig. 2). Thus, we presume this mesoporous material has a band structure composed of Si  $3p$  (near the CB edge) and O  $2p$  levels (above the VB edge) (Fig. 10(a)). On the other hand, when  $\text{TiO}_2$  nanocrystals were incorporated into this SBA-15 mesoporous, there is also the effective participation of Ti  $3d$  levels within the forbidden region (Fig. 10(b)). In this structure, it is possible a correlation between tetrahedral  $[\text{SiO}_4]$  clusters and distorted octahedral  $[\text{TiO}_6]$  clusters.

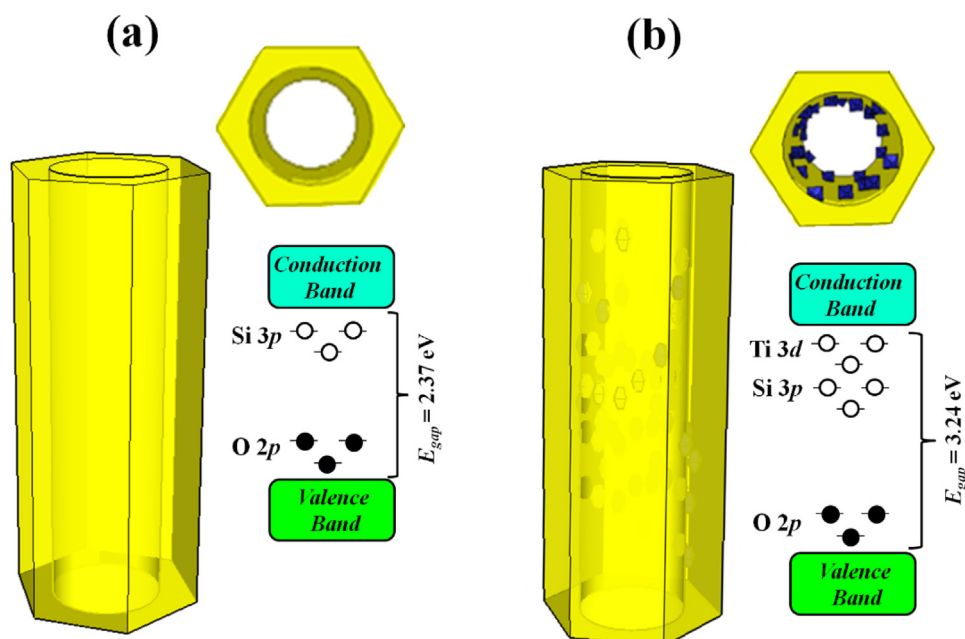
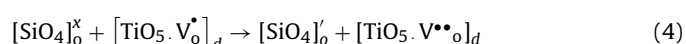
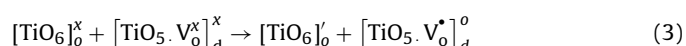


Fig. 10. Schematic representation of optical band gap model for: (a) pure SBA-15 and (b) TiO<sub>2</sub>/SBA-15.

In cases involving electronic conduction properties, these clusters are able to present a cluster-to-cluster charge transfer (CCCT) from SiO<sub>2</sub> (SBA-15) to TiO<sub>2</sub> (or vice-versa) by means of excitations involving electronic transitions [85]. This CCCT mechanism induces the formation of different energy levels within the forbidden band gap (effect of structural order/disorder). Particularly, this phenomenon has its origin during the crystal formation and organization stages, which are directly dependent on interactions between tetrahedral [SiO<sub>4</sub>] clusters and distorted octahedral [TiO<sub>6</sub>] clusters. Therefore, these structural defects promote a symmetry break, causing a polarization in the structure by the electronic charge transfer from ordered (*o*) to disordered (*d*) clusters (formation of electron-hole pairs), which can be explained by the following equations (1–5):



where, [SiO<sub>4</sub>]<sub>d</sub><sup>x</sup>, [TiO<sub>6</sub>]<sub>d</sub><sup>x</sup> and [TiO<sub>5</sub>·V<sub>o</sub><sup>x</sup>]<sub>d</sub> are electron donors, [TiO<sub>5</sub>·V<sub>o</sub><sup>x</sup>]<sub>d</sub> is electron donors/acceptors and [SiO<sub>4</sub>]<sub>o</sub><sup>x</sup> and [TiO<sub>6</sub>]<sub>o</sub><sup>x</sup> are electron acceptors.

#### 4. Conclusion

In summary, pure SBA-15 mesoporous, anatase TiO<sub>2</sub> nanocrystals and anatase TiO<sub>2</sub> nanocrystals anchored into the mesoporous of SBA-15 matrix were obtained with success by the reflux and hydrothermal methods, respectively. XRD patterns, and Micro-Raman spectra indicated TiO<sub>2</sub> nanocrystals have a tetragonal structure and space group (*I4<sub>1</sub>/amd*). The pure SBA-15 matrix exhibited typical XRD peaks at low angle of SiO<sub>2</sub> amorphous and SiO<sub>2</sub> mesoporous. These results are in agreement with highly ordered 2D hexagonal mesostructures with space group *P6mm*. XRD peaks at wide angle and Raman-active vibration modes

found for anatase TiO<sub>2</sub> nanocrystals anchored into the mesoporous of SBA-15 matrix were only assigned to tetragonal structure of anatase TiO<sub>2</sub> nanocrystals. FT-IR spectra exhibited typical IR-active vibrational modes of tetrahedral [SiO<sub>4</sub>] clusters. Moreover, there is a strong chemical bond (HO–Si–O–Ti–O) presents between octahedral [TiO<sub>6</sub>] clusters in TiO<sub>2</sub> nanocrystals with the tetrahedral [SiO<sub>4</sub>] clusters of SBA-15. FE-SEM images showed the decrease of Si/Ti molar ratios promoted changes in the growth direction as well as in the elongated hexagon-like SBA-15 shapes. TEM and HRTEM images showed the presence of micropores and 2D hexagonal mesopores of SBA-15. In addition, anatase TiO<sub>2</sub> nanocrystals anchored into the mesoporous of SBA-15 material were estimated with observation of TEM images and textural analyses. BET and BJH methods indicated the decrease of Si/Ti molar ratio is an ideal condition to promote an increase in the wall thickness. Finally, UV–vis diffuse reflectance spectroscopy indicated an increase in optical band gap energy values (from 2.37 to 3.24 eV) with the increase of molar ratios. This phenomenon was attributed to the formation of additional electronic energy levels arising from Ti 3*d* orbitals according our optical band gap model.

#### Acknowledgments

The Brazilian authors acknowledge the financial support of the Brazilian research financing institutions: LIMAV-UFPI, IFPI, UERN, CNPq (307559/2015-7; 350711/2012-7; 479644/2012-8; 455864/2014-4), FAPESP (12/14004-5; 13/07296-2) and CAPES (33001014005P5); CAPES/PNPD (20131475).

#### Appendix A. Supplementary data

Supplementary data associated with this article can be found, in the online version, at <http://dx.doi.org/10.1016/j.apsusc.2016.08.018>.

#### References

- [1] T. Yanagisawa, T. Shimizu, K. Kuroda, C. Kato, The preparation of alkyltriinethylinoninium–kaneite complexes and their conversion to microporous materials, *Bull. Chem. Soc. Jpn.* 63 (1990) 988–990.

- [2] J.S. Beck, J.C. Vartuli, W.J. Roth, M.E. Leonowicz, C.T. Kresge, K.D. Schmitt, C.T.W. Chu, D.H. Olson, E.W. Sheppard, A new family of mesoporous molecular sieves prepared with liquid crystal templates, *J. Am. Chem. Soc.* 114 (1992) 10834–10843.
- [3] B.G. Trewyn, I.I. Slowing, S. Giri, H.T. Chen, V.S.Y. Lin, Synthesis and functionalization of a mesoporous silica nanoparticle based on the sol–gel process and applications in controlled release, *Acc. Chem. Res.* 47 (2007) 846–885.
- [4] D. Zhao, J. Feng, Q. Huo, N. Melosh, G.H. Fredrickson, B.F. Chmelka, G.D. Stucky, Triblock copolymer syntheses of mesoporous silica with periodic 50–300 angstrom pores, *Science* 279 (1998) 548–552.
- [5] V.F. Vavsari, G.M. Ziarani, A. Badieic, The role of SBA-15 in drug delivery, *RSC Adv.* 5 (2015) 91686–91707.
- [6] Z. Bagheryan, J.B. Raouf, R. Ojani, P. Rezaei, Development of a new biosensor based on functionalized SBA-15 modified screen-printed graphite electrode as a nano-reactor for Gquadruplex recognition, *Talanta* 119 (2014) 24–33.
- [7] T. Kadoono, M. Ogura, Heat storage properties of organic phase-change materials confined in the nanopore of mesoporous SBA-15 and CMK-3, *Phys. Chem. Chem. Phys.* 28 (2014) 5495–5498.
- [8] Q.Z. Zhai, S.J. Sun, Preparation characterization, and luminescence of (SBA-15) immobilized pepsin, *Photochem. Magnetochem. Russian J. Phys. Chem. A.* 88 (2014) 2243–2251.
- [9] Q.F. Li, D. Yue, W. Lu, X. Zhang, C. Li, Z. Wang, Hybrid luminescence materials assembled by [Ln(DPA)<sub>3</sub>]<sub>3</sub>- and mesoporous host through ion-pairing interactions with high quantum efficiencies and long lifetimes, *Sci. Rep.* 5 (2015) 8385–8394.
- [10] A. de Sousa, K.C. de Souza, P.M.S. Leite, R.G. de Sousa, E.M.B. de Sousa, A dual-functional [SBA-15/Fe<sub>3</sub>O<sub>4</sub>/P(N-iPAAm)] hybrid system as a potential nanoplatform for biomedical application, *J. Nanomater.* 2014 (2014) 293624–293633.
- [11] J.A. Shusterman, H.E. Mason, J. Bowers, A. Bruchet, E.C. Uribe, A.B. Kersting, H. Nitsche, Development and testing of diglycolamide functionalized mesoporous silica for sorption of trivalent actinides and lanthanides, *ACS Appl. Mater. Interfaces* 7 (2015) 20591–20599.
- [12] J. Zhu, K. Kailasam, X. Xie, R. Schomaecker, A. Thomas, High-surface-area SBA-15 with enhanced mesopore connectivity by the addition of poly(vinyl alcohol), *Chem. Mater.* 23 (2011) 2062–2067.
- [13] A.O. Jorgetto, S.P. Pereira, R.I.V. da Silva, M.J. Saeki, M.A.U. Martines, V.A. Pedrosa, G.R. de Castro, Application of mesoporous SBA-15 silica functionalized with 4-amino-2-mercaptopyrimidine for the adsorption of Cu (II), Zn (II), Cd (II), Ni (II) and Pb (II) from water, *Acta Chim. Slov.* 62 (2015) 111–121.
- [14] S. Wang, K. Wang, C. Dai, H. Shi, J. Li, Adsorption of Pb<sup>2+</sup> on amino-functionalized core–shell magnetic mesoporous SBA-15 silica composite, *Chem. Eng. J.* 262 (2015) 897–903.
- [15] C.Z. Wen, H.B. Jiang, S.Z. Qiao, H.G. Yang, G.Q.M. Lu, Synthesis of high-reactive facets dominated anatase TiO<sub>2</sub>, *J. Mater. Chem.* 21 (2011) 7052–7061.
- [16] Y. Zhang, X. Pu, Y. Yang, Y. Zhu, H. Hou, M. Jing, X. Yang, J. Chen, X. Ji, An electrochemical investigation of rutile TiO<sub>2</sub> microspheres anchored by nanoneedle clusters for sodium storage, *Phys. Chem. Chem. Phys.* 17 (2015) 15764–15770.
- [17] Y. Liu, Y. Luo, A.A. Elzathary, W. Luo, R. Che, J. Fan, K. Lan, A.M. Al-Enizi, Z. Sun, B. Li, Z. Liu, D. Shen, Y. Ling, C. Wang, J. Wang, W. Gao, C. Yao, K. Yuan, H. Peng, Y. Tang, Y. Deng, G. Zheng, G. Zhou, D. Zhao, Mesoporous TiO<sub>2</sub> mesocrystals: remarkable defects-induced crystallite–interface reactivity and their in situ conversion to single crystals, *ACS Cent. Sci.* 1 (2015) 400–408.
- [18] T.J. Bastow, G. Doran, H.J. Whitfield, Electron diffraction and <sup>47,49</sup>Ti and <sup>17</sup>O NMR studies of natural and synthetic brookite, *Chem. Mater.* 12 (2000) 436–439.
- [19] E. Filippo, C. Carlucci, A.L. Capodilupo, P. Perulli, F. Conciauro, G.A. Corrente, G. Gigli, G. Ciccarella, Enhanced photocatalytic activity of pure anatase TiO<sub>2</sub> and Pt-TiO<sub>2</sub> nanoparticles synthesized by green microwave assisted route, *Mater. Res.* 18 (2015) 473–481.
- [20] S. Bagheri, N.M. Julkapli, S.B.A. Hamid, Titanium dioxide as a catalyst support in heterogeneous catalysis, *Sci. World J.* 2014 (2014) 727496–727517.
- [21] V.K. Tomer, S. Duhan, Nano titania loaded mesoporous silica: preparation and application as high performance humidity sensor, *Sens. Actuators B: Chem.* 220 (2015) 192–200.
- [22] Y. Chen, J. Wang, W. Li, M. Ju, Microwave-assisted hydrothermal synthesis of Au/TiO<sub>2</sub>/SBA-15 for enhanced visible-light photoactivity, *Mater. Lett.* 159 (2015) 131–134.
- [23] L. Liang, Y. Meng, L. Shi, J. Ma, J. Sun, Enhanced photocatalytic performance of novel visible light-driven Ag–TiO<sub>2</sub>/SBA-15 photocatalyst, *Superlattices Microstruct.* 73 (2014) 60–70.
- [24] V. Sazo, C.M. López, M. De Quesada, J.M. Vieira, Synthesis of TiSBA-15 with low HCl content as catalysts in cyclohexene epoxidation, *Catal. Today* 172 (2011) 8–12.
- [25] L.Y. Hong, S.Y. Oh, A. Matsuda, C.S. Lee, D.P. Kim, Hydrophilic and mesoporous SiO<sub>2</sub>–TiO<sub>2</sub>–SO<sub>3</sub>H system for fuel cell membrane applications, *Electrochim. Acta* 56 (2011) 3108–3114.
- [26] C.L. Peza-Ledesma, L. Escamilla-Perea, R. Nava, B. Pawelec, J.L.G. Fierro, CO oxidation at 20 °C over Au/SBA-15 catalysts decorated by Fe<sub>2</sub>O<sub>3</sub> nanoparticles, *Catal. Commun.* 15 (2011) 108–112.
- [27] C.H. Liu, Y. Guan, E.J.M. Hensen, J.F. Lee, C.M. Yang, Au/TiO<sub>2</sub>@SBA-15 nanocomposites as catalysts for direct propylene epoxidation with O<sub>2</sub> and H<sub>2</sub> mixtures, *J. Catal.* 282 (2011) 94–102.
- [28] M.M. Wan, X.D. Sun, S. Liu, J. Ma, J.H. Zhu, Versatile drug releaser derived from the Ti-substituted mesoporous silica SBA-15, *Microporous Mesoporous Mater.* 199 (2014) 40–49.
- [29] Y.J. Acosta-Silva, R. Nava, V. Hernández-Morales, S.A. Macías-Sánchez, M.L. Gómez-Herrera, B. Pawelec, Methylene blue photodegradation over titania-decorated SBA-15, *Appl. Catal. B: Environ.* 110 (2011) 108–117.
- [30] R. Huirache-Acuña, R. Nava, C.L. Peza-Ledesma, J. Lara-Romero, G. Alonso-Núñez, B. Pawelec, E.M. Rivera-Muñoz, SBA-15 mesoporous silica as catalytic support for hydrodesulfurization catalysts, *Materials* 6 (2013) 4139–4167.
- [31] T.P.T. Thi, D.T. Nguyen, T.Q. Duong, H.H. Luc, V. Vo, Facile postsynthesis of n-doped TiO<sub>2</sub>–SBA-15 and its photocatalytic activity, *Adv. Mater. Sci. Eng.* 2013 (2013) 638372–638379.
- [32] J. Feng, G. An, B. Chen, Y. Li, K. Ding, Y. Xie, Z. Liu, Post-synthesis of Ti-SBA-15 in supercritical CO<sub>2</sub>–ethanol solution, *CLEAN – Soil, Air, Water* 37 (2009) 527–533.
- [33] Z. Shu-Cui, J. Dong, T. Tao, L. Jun-Hua, X. Yao, Synthesis and photocatalytic activity of highly dispersed TiO<sub>2</sub>/SBA-15, *Acta Phys.-Chim. Sin.* 26 (2010) 1330–1336.
- [34] N.P. Hung, N.T.V. Hoan, N.V. Nghia, Synthesis and characterization of photocatalytic material TiO<sub>2</sub>/SBA-15, *Nanosci. Nanotechnol.* 3 (2013) 19–25.
- [35] P.T. Dang, H.G. Le, D.V. Hoang, Y. Hoang, T.C. Dinh, L.H. Bui, H.T.K. Tran, P.H. Nguyen, T.A. Vu, Synthesis, characterization, and catalytic properties of Ti-containing SBA-15 mesoporous materials, *Proc. of SPIE* (2006) 64151–64160.
- [36] J. Yang, J. Zhang, L. Zhu, S. Chen, Y. Zhang, Y. Tang, Y. Zhu, Y. Li, Synthesis of nano titania particles embedded in mesoporous SBA-15: characterization and photocatalytic activity, *J. Hazard. Mater.* 137 (2006) 952–958.
- [37] S. Zhang, D. Jiang, T. Tang, J. Li, Y. Xu, W. Shen, J. Xu, F. Deng, TiO<sub>2</sub>/SBA-15 photocatalysts synthesized through the surface acidolysis of Ti (OnBu)<sub>4</sub> on carboxyl-modified SBA-15, *Catal. Today* 158 (2010) 329–335.
- [38] X.J. Wang, F.T. Li, Y.J. Hao, S.J. Liu, M.L. Yang, TiO<sub>2</sub>/SBA-15 composites prepared using H<sub>2</sub>TiO<sub>3</sub> by hydrothermal method and its photocatalytic activity, *Mater. Lett.* 99 (2013) 38–41.
- [39] L. Yang, Z. Jiang, S. Lai, C. Jiang, H. Zhong, Synthesis of titanium containing SBA-15 and its application for photocatalytic degradation of phenol, *Int. J. Chem. Eng. 2014 (2014) 691562–691568.*
- [40] Y. Chen, Y. Huang, J. Xiu, X. Han, X. Bao, Direct synthesis: characterization and catalytic activity of titanium-substituted SBA-15 mesoporous molecular sieves, *Appl. Catal. A: Gen.* 273 (2004) 185–191.
- [41] P.V. Messina, P.C. Schulz, Adsorption of reactive dyes on titania/silica mesoporous materials, *J. Colloid Interface Sci.* 299 (2006) 305–320.
- [42] T. Hoshikawa, T. Ikebe, M. Yamada, R. Kikuchi, K. Eguchi, Preparation of silica-modified TiO<sub>2</sub> and application to dye-sensitized solar cells, *J. Photochem. Photobiol. A: Chem.* 184 (2006) 78–85.
- [43] G.E. Luz Jr., A.G.D. Santos, A.C.R. Melo, R.M. Oliveira, A.S. Araújo, V.J. Fernandes Jr., Thermal catalytic cracking of buriti oil (*Mauritia flexuosa* L.) over LaSBA-15 mesoporous materials, *Fuel Process. Technol.* 92 (2011) 2099–2104.
- [44] G.E. Luz Jr., S.H. Lima, A.C.R. Melo, A.S. Araújo, V.J. Fernandes Jr., Direct synthesis and characterization of LaSBA-15 mesoporous molecular sieves, *J. Mater. Sci.* 45 (2010) 1117–1122.
- [45] S. Brunauer, P.H. Emmett, E. Teller, Adsorption of gases in multimolecular layers, *J. Am. Chem. Soc.* 60 (1938) 309–319.
- [46] E.P. Barrett, L.G. Joyner, P.P. Halenda, The determination of pore volume and area distributions in porous substances. I. Computations from nitrogen isotherms, *J. Am. Chem. Soc.* 73 (1951) 373–380.
- [47] P. Kubelka, F. Munk, Ein Beitrag zur optik der farbanstriche, *Zeit Für Tech Physik* 12 (1931) 593–601.
- [48] R. Salh, Defect Related Luminescence in Silicon Dioxide Network: A Review, *Cap. 8, 2015, 152–155.*
- [49] T. Kang, Y. Park, K. Choi, J.S. Lee, J. Yi, Ordered mesoporous silica (SBA-15) derivatized with imidazole-containing functionalities as a selective adsorbent of precious metal ions, *J. Mater. Chem.* 14 (2004) 1043–1049.
- [50] Y.J. Han, J.M. Kim, G.D. Stucky, Preparation of noble metal nanowires using hexagonal mesoporous silica SBA-15, *Chem. Mater.* 12 (2000) 2068–2069.
- [51] I.C. Nogueira, L.S. Cavalcante, P.F.S. Pereira, M.M. de Jesus, J.M. Rivas Mercury, N.C. Batista, M. Siu Li, E. Longo, Rietveld refinement: morphology and optical properties of (Ba<sub>1-x</sub>Sr<sub>x</sub>) MoO<sub>4</sub> crystals, *J. Appl. Cryst.* 46 (2013) 1434–1446.
- [52] V.K. Tomer, S. Jangra, R. Malik, S. Duhan, Effect of in-situ loading of nano titania particles on structural ordering of mesoporous SBA-15 framework, *Coll. Surf. A* 466 (2015) 160–165.
- [53] I. Djerdj, A.M. Tonejc, Structural investigations of nanocrystalline TiO<sub>2</sub> samples, *J. Alloys Compd.* 413 (2006) 159–174.
- [54] H. Song, R.M. Rioux, J.D. Hoefelmeyer, R. Komor, K. Niesz, M. Grass, P. Yang, G.A. Somorjai, Hydrothermal growth of mesoporous SBA-15 silica in the presence of PVP-stabilized Pt nanoparticles: synthesis, characterization, and catalytic properties, *J. Am. Chem. Soc.* 128 (2006) 3027–3037.
- [55] N. Hamilton, T. Wolfram, G.T. Müller, M. Hävecker, J. Kröhnert, C. Carrero, R. Schomäcker, A. Trunschke, R. Schlögl, Topology of silica supported vanadium–titanium oxide catalysts for oxidative dehydrogenation of propane, *Catal. Sci. Technol.* 2 (2012) 1346–1359.
- [56] Y. Borodko, J.W. Ager III, G.E. Marti, H. Song, K. Niesz, G.A. Somorjai, Structure sensitivity of vibrational spectra of mesoporous silica SBA-15 and Pt/SBA-15, *J. Phys. Chem. B.* 109 (2005) 17386–17390.

- [57] X. Fan, J. Li, Z. Zhao, Y. Wei, J. Liu, A. Duan, G. Jiang, Dehydrogenation of propane over PtSn/SBA-15 catalysts: effect of the amount of metal loading and state, *RSC Adv.* 5 (2015) 28305–28315.
- [58] J. Yan, G. Wu, N. Guan, L. Li, Z. Li, X. Cao, Understanding the effect of surface/bulk defects on the photocatalytic activity of TiO<sub>2</sub>: anatase versus rutile, *Phys. Chem. Chem. Phys.* 15 (2013) 10978–10988.
- [59] G.J. Exarhos, N.J. Hess, S. Ryan, Laser Raman measurements of dielectric coatings as a function of temperature, *SPIE Proc.* 1441 (1990) 190–199.
- [60] W.F. Zhang, Y.L. He, M.S. Zhang, Z. Yin, Q. Chen, Raman scattering study on anatase TiO<sub>2</sub> nanocrystals, *J. Phys. D.: Appl. Phys.* 33 (2000) 912–916.
- [61] H.C. Choi, Y.M. Jung, S.B. Kim, Size effects in the Raman spectra of TiO<sub>2</sub> nanoparticles, *Vib. Spectrosc.* 37 (2005) 33–38.
- [62] I. Cesarino, G. Marino, J.R. Matos, E.T.G. Cavalheiro, Using the organofunctionalised SBA-15 nanostructured silica as a carbon paste electrode modifier: determination of cadmium ions by differential anodic pulse stripping voltammetry, *J. Braz. Chem. Soc.* 18 (2007) 810–817.
- [63] Z. Wang, F. Zhang, Y. Yang, B. Xue, J. Cui, N. Guan, Facile postsynthesis of visible-light-sensitive titanium dioxide/mesoporous SBA-15, *Chem. Mater.* 19 (2007) 3286–3293.
- [64] M. Vallet-Regí, M. Manzano, J.M. González-Calbet, E. Okunishid, Evidence of drug confinement into silica mesoporous matrices by STEM spherical aberration corrected microscopy, *Chem. Commun.* 43 (2010) 2956–2958.
- [65] D. Jung, C. Streb, M. Hartmann, Covalent anchoring of chloroperoxidase and glucose oxidase on the mesoporous molecular sieve SBA-15, *Int. J. Mol. Sci.* 11 (2010) 762–778.
- [66] S. Rasalingam, R. Peng, R.T. Koodali, Removal of hazardous pollutants from wastewaters: applications of TiO<sub>2</sub>-SiO<sub>2</sub> mixed oxide materials, *J. Nanomater.* 2014 (2014) 1–42.
- [67] Y. Liu, Z. Liu, J. Gao, J. Dai, J. Han, Y. Wang, J. Xie, Y. Yan, Selective adsorption behavior of Pb (II) by mesoporous silica SBA-15-supported Pb (II)-imprinted polymer based on surface molecularly imprinting technique, *J. Hazard. Mater.* 186 (2011) 197–205.
- [68] A. de Sousa, K.C. de Souza, P.M.S. Leite, R.G. de Sousa, E.M.B. de Sousa, A dual-functional [SBA-15/Fe<sub>3</sub>O<sub>4</sub>/P(N-iPAAM)] hybrid system as a potential nanoplatform for biomedical application, *J. Nanomater.* 2014 (2014) 293624–293633.
- [69] M.S. Asgari, A. Zonouzi, R. Rahimi, M. Rabbani, Application of porphyrin modified sba-15 in adsorption of lead ions from aqueous media, *Orient. J. Chem.* 31 (2015) 1537–1544.
- [70] K.S.W. Sing, D.H. Everett, R.A.W. Haul, L. Moscow, R.A. Pierotti, J. Rouquerol, T. Siemieniewska, Reporting physisorption data for gas/solid systems with special reference to the determination of surface area and porosity, *Pure Appl. Chem.* 57 (1985) 603–619.
- [71] T. Gondo, K. Kaneko, T. Nishiyama, K. Yamada, Z. Saghi, J.S. Barnarda, P.A. Midgley, Microstructural analysis of Au/TiO<sub>2</sub>-SBA-15 nanocomposite, *Microsc. Microanal.* 20 (2014) 1001–1007.
- [72] Y. Han, S.B. Kim, H. Kim, TiO<sub>2</sub>-coated silica foams by in-situ sol-gel reaction, *Mater. Trans.* 52 (2011) 2245–2249.
- [73] P. Linton, V. Alfredsson, Growth and morphology of mesoporous SBA-15 particles, *Chem. Mater.* 20 (2008) 2878–2880.
- [74] H. Fan, C. Hartshorn, T. Buchheit, D. Tallant, R. Assink, R. Simpson, D.J. Kissel, D.J. Lacks, S. Torquato, C.J. Brinker, Modulus–density scaling behaviour and framework architecture of nanoporous self-assembled silicas, *Nature Mater.* 6 (2007) 418–423.
- [75] F. Chang, G. Wang, Y. Xie, M. Zhang, J. Zhang, H.J. Yang, X. Hu, Synthesis of TiO<sub>2</sub> nanoparticles on mesoporous aluminosilicate Al-SBA-15 in supercritical CO<sub>2</sub> for photocatalytic decolorization of methylene blue, *Ceram. Int.* 39 (2013) 3823–3829.
- [76] M. Halder, Determination of the critical micellar concentration (CMC) of a cationic micelle from stokes shift data, *Chem. Educ.* 12 (2007) 33–36.
- [77] F. Hoffmann, M. Cornelius, J. Morell, M. Froba, Silica-based mesoporous organic–inorganic hybrid materials, *Angew. Chem. Int. Ed.* 45 (2006) 3216–3251.
- [78] R. Zana, C. Marques, A. Johner, Dynamics of micelles of the triblock copolymers poly (ethylene oxide)–poly (propylene oxide)–poly (ethylene oxide) in aqueous solution, *Adv. Colloid Interface Sci.* 123–126 (2006) 345–351.
- [79] P. Mukherjee, The nature of the association equilibria and hydrophobic bonding in aqueous solutions of association colloids, *Adv. Colloid Interface Sci.* 1 (1967) 242–275.
- [80] R.G. Laughlin, *The Aqueous Phase Behaviour of Surfactants*, 6th ed., Academic Press., London, 1994, pp. 203–208.
- [81] D.F. Evans Fennell, H. Wennerström, *The Colloidal Domain*, 2nd, Wiley VCH, New York, 1999, pp. 219–220.
- [82] V. Alfredsson, H. Wennerström, The dynamic association processes leading from a silica precursor to a mesoporous SBA-15 material, *Acc. Chem. Res.* 48 (2015) 1891–1900.
- [83] J. Ma, J. Chu, L. Qiang, J. Xue, Effect of different calcination temperatures on the structural and photocatalytic performance of Bi-TiO<sub>2</sub>/SBA-15, *Int. J. Photoenergy* 2013 (2013) 875456–875465.
- [84] C. Zhao, L. Liu, Q. Zhang, J. Wang, Y. Li, Photocatalytic conversion of CO<sub>2</sub> and H<sub>2</sub>O to fuels by nanostructured Ce-TiO<sub>2</sub>/SBA-15 composites, *Catal. Sci. Technol.* 2 (2012) 2558–2568.
- [85] L.S. Cavalcante, V.M. Longo, J.C. Sczancoski, M.A.P. Almeida, A.A. Batista, J.A. Varela, M.O. Orlandi, E. Longo, M. Siu Li, Electronic structure: growth mechanism and photoluminescence of CaWO<sub>4</sub> crystals, *CrystEngComm* 14 (2012) 853–868.